Journal of Advanced Joining Processes 5 (2022) 100109

Contents lists available at ScienceDirect

Journal of Advanced Joining Processes

journal homepage: www.sciencedirect.com/journal/journal-of-advanced-joining-processes

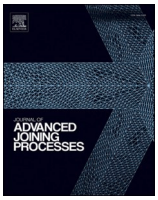

Investigation of the mechanical properties and corrosion behaviour of hybrid L 80 Type 1 and duplex steel joints produced by magnetically impelled arc butt welding

Thomas Hassel [a,*], Hans Jürgen Maier [a], Alexey Alkhimenko [b], Artem Davydov [b], Nikita Shaposhnikov [b], Gleb Turichin [c], Olga Klimova [c]

[a] Leibniz Universitat Hannover Fakultat fur Maschinenbau Garbsen, Low Saxonia, Germany
[b] Peter the Great St. Petersburg Polytechnic University, Saint Petersburg, Russia
[c] State Marine University, Sankt Petersburg, Russia

ARTICLE INFO

Keywords:
Geothermal wells
Borehole casing
Tube welding
Magnetically impelled arc butt welding (MIAB)
Hybrid joining

ABSTRACT

In the field of deep geothermal energy, the mono-tube design will be increasingly used in the future, as significant cost savings can be expected in the production of boreholes up to depths of 6000 m. The previously used bolting of the pipe lengths by means of sleeves contributes significantly to the construction costs. In addition, there is an increased risk of failure for the sleeve bolting, especially if different materials have to be used in different layers for the purpose of increasing the corrosion resistance. Magnetically Impelled Arc Butt Welding (MIAB) was used for direct welding of pipe segments with complete elimination of socket bolting. In the process, the casing material (L80 Type 1), which is a cost-effective standard material, and a corrosion-resistant duplex steel (1.4462) were hybrid welded. The results show excellent properties both in terms of mechanical properties and corrosion resistance. It is shown that the advantages of the MIAB process in joining these different materials can successfully overcome the metallurgical challenges. This new approach for the production of borehole liners can contribute significantly to cost reduction in the construction of geothermal boreholes.

Introduction

Despite the increasing use of sustainable energy types to meet our energy demands, exploration efforts through drilling will continue to be necessary. In particular, classical drilling technology will remain indispensable for the development of deep geothermal reservoirs in the future (JFE Steel Corporation 2021). Since the economic viability of drilling has so far been strongly linked to the exploitation potential of the raw materials to be extracted, geothermal wells will have to undergo a substantial cost reduction in well construction in order to meet future economic constraints (Fruhwirth and Hofstätter 2016). The conventional method of drilling a deep borehole is currently still very conservative and takes the form of a borehole with a telescopically decreasing diameter. The drilling is started with a multiple of the intended borehole diameter in order to provide the different sections with appropriate concrete linings to stabilize the borehole. The diameter of each subsequent drilling section is thus reduced so that at the target depth it is possible to work with the intended production cross-section. This method, which has been in use for decades, is the one most commonly used today because it has produced the most stable results so far. A more recent development is the mono borehole design, which can be used to achieve deep boreholes of several thousand meters with a constant diameter, and thus almost the production cross section can be realized over the entire distance (Teodoriu 2015).

One of the major cost drivers in well construction is the well lining and production tubing tour, which is done using steel tubing. Casing pipes inserted into the borehole prevent the borehole from collapsing, and thus stabilize the production cross section. The medium is then conveyed over the operating time via the production pipe tours carried out (Galle et al., 2011).

The depth of boreholes can be up to 6000 m, which means that the high number of connections of the pipe tours represents a considerable cost factor. The probability of failure of the many fittings increases the risk of leaks along the entire pipe tour. The steel tubes of the casing construction have a wall thickness of approx. 11 to 13 mm and a diameter of approx. 500 mm for the first one hundred meters of the

* Corresponding author.
E-mail address: hassel@iw.uni-hannover.de (T. Hassel).

https://doi.org/10.1016/j.jajp.2022.100109
Received 10 February 2022; Received in revised form 26 March 2022; Accepted 26 March 2022
Available online 14 April 2022

borehole. Due to the telescopic tapering with increasing depth, the casing diameter is then reduced, for example, to 340 mm up to 1700 m depth, 178 mm and 245 mm up to 4748 m depth and finally to 140 mm at the deepest range of 1748 to 6248 m. Thus, for one well, 11,070 m of casing is installed in the 340 to140 mm diameter range (Sun et al., 2012).

In addition, the environment water surrounding the pipeline typically changes considerably depending on the depth, so that it is necessary to react to corrosive media with a specific choice of material for the casing (Li et al., 2012; Li 2013a, 2013b; Davydov et al., 2020; Sedmak et al., 2020). Up to now, the casing pipes are installed using screwed socket connectors. For this purpose, threaded pieces are attached to the pipe ends (friction-welded precision threaded pieces). A threaded socket is then screwed on during installation. This creates a connection with seals between the 10 to 16 m long pipe sections (casings), cf. Fig. 1(a).

Disadvantages of this technology are, on the one hand, the cost-intensive production of the threaded pieces and the necessary friction welding to the pipe sections as well as the production of the couplings themselves. In addition, the installation of the pipes on the rig is a bottleneck in the drilling process, since even slight damage to the threaded connections is intolerable. In addition, the bending radius of a pipe connected by joints has to be large and bending can lead to leaks if the limits are exceeded. There are also geometric limitations, since the socket is an interference point in the outer contour of the casing pipe, and jamming can occur upon sinking of the segment.

Another major disadvantage is that in areas of the wells subject to high corrosive attack (e. g. due to H_2S and CO_2) (Alkhimenko 2019; Kostitsyna et al., 2019), sleeve connectors made of Ni-based alloys must be used, which, although stable against corrosion itself, can form galvanic elements when in contact with the steel casing. This accelerates corrosion, and thus increases the probability of failure with reduced service life of the borehole (Ren et al., 2012; Alekseeva et al., 2020).

Unalloyed and low-alloy materials as well as high-alloy steels are generally used as pipe materials. Table 1) shows the different compositions of steels from the L80 material group as well as their mechanical properties and dimensions. The L80 is used more often when exposure to hydrogen sulphide is dominant, and the Cr-alloyed types, 9Cr-L80 and 13-L80 are used for regions where exposure to carbon dioxide is the key issue. If different corrosion media prevail at different depths, a material mix of the different grades must be used in the casing.

Another, much simpler method of connecting the individual pipes would be direct welding of the casing pipes, see Fig. 1(b), which is already employed in cavern construction using manual welding (Oppelt and Lehr 2012). In this case, no sockets or threaded connectors are required, which is a significant process improvement. A disadvantage is that the weld structure of a fusion weld always has worse properties than the base material, so that the weld seams are the weak points in the casing strand (Bérest et al., 2019). In addition, mixed joints, e. g. of non-alloyed and alloyed steel, are a challenge, since the mixing upon welding of the materials often leads to a deterioration of the material

Fully automated variants for friction welding using a friction disk and conductive pressure welding are currently being developed for producing the casing directly on the drilling rig. Friction welding with a rotating friction disk uses a rotating friction body between the clamped casing tubes. The rotation of the friction disk and the acting friction pressure generate heat at the contact surfaces. As the friction disk rotates, the two end faces are pressed against it. The resulting frictional heat leads to softening of the friction disk and tube material. During further pressing, the material of the friction disk is displaced into the friction ridge. The joining process ends with the complete "rubbing through" of the friction disk. The resulting friction and upset burr is separated while still in the soft state (Faes et al., 2007; Faes et al., 2009).

A different approach is to form welded joints by press butt welding using an active shielding gas cover. In this process, which resembles forge welding, the pipes are inductively or conductively heated in a fixed clamp under shielding gas cover. The pipe faces are then pressed onto each other, and it is reported that these joints have increased torsional strength compared to threaded connectors (Ganesan et al., 2010; Moe et al., 2010; Vinothkumar et al., 2011; Palanisamy et al., 2021).

Another process very well suited for welding tubes is MIAB pressure welding (Vendan et al., 2012). When using the MIAB-PW process, the welding arc moves under the influence of a Lorenz force generated by an external constant magnetic field, which moves the arc radially around the end faces of the pipe ends. This welding process is mainly used in industry for joining parts with tubular cross-sections with wall thicknesses of up to 4 mm and outer diameters of up to 10 mm for the automotive industry using shielding gases. For substantially larger tubes, an industrial application has not yet been realized due to a lack of information on the mechanical properties and corrosion resistance (Kovalev et al., 2020) of the welded joints. However, the excellent weld quality that was realized with MIAB of small tubes, has triggered substantial efforts to produce joints of pipes with 10–20 mm wall thickness made of high-strength steels with a diameter of up to 320 mm (Kachinskiy et al., 2002; Varahram et al., 2014; Hassel et al., 2016a; Hassel et al., 2016b; Kachinsky and Kuchuk-Yatsenko 2017). The present study addresses the properties of hybrid joints formed via MIAB, which is a key issue for using this technology for deep drilling applications.

As a classic welding process for pipe joints, the MIAB process represents a way to act quickly and economically in pipeline construction. Continuous research is also being carried out on the process, especially in the area of process control and the application of machine learning, there is considerable development potential for this method (Panda et al., 2017; Vendan et al., 2020). For example, Dhivyasri et al. address the issue of optimising the process through detailed control of welding current and welding time. Through the development of a double PID feedback controller, this leads to an optimisation of welding current and welding time through a fast process-integrated set-point tracking (Dhivyasri et al., 2018). Balte et al. presents a comparison between rotation friction welding and the MIAB process and compares the microstructural formation as well as the mechanical properties using the example of unalloyed steels with up to 0.5% carbon content. In MIAB welding, this leads to a limited burn-off of carbon in the heating phase and a decarburised zone is observed in the middle of the weld zone during the welding tests, but this zone is <10 µm wide and has no influence on the mechanical properties (Berna Balta et al., 2018). The results of Suresh et al. show that MIAB-welded specimens have excellent structural properties of piping systems, with the added benefit of improved

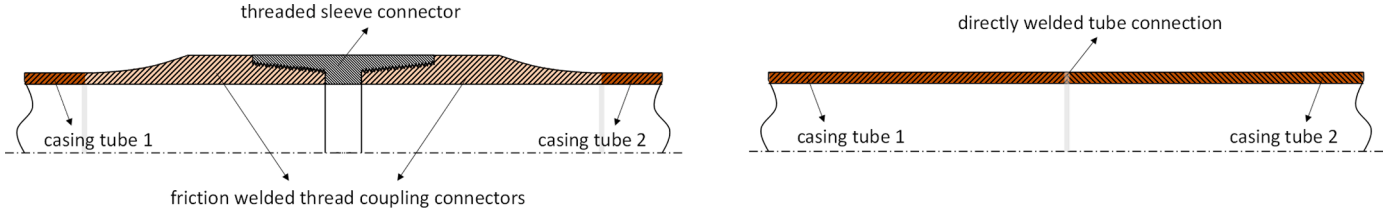

Fig. 1. Schematic illustration of the connection principle of casing pipes in drilling technology; a: connection via the use of threaded sockets; b: connection using direct welding of the pipes during installation.

Table 1
Compilation of commercially available materials used in drilling technology for casing and tubing; chemical compositions are given in wt.-% (TPS technitube Röhrenwerke GmbH 2017; API American Petroleum Institute 2021).

chemical composition														mechanical properties			dimensions	
material	element	C	Mn	Mo	Cr	Ni	Cu	Ti	P	S	Si	N	Al		minimum	maximum	casing OD/ wall thickness (d)	tubing OD/ wall thickness (d)
L80*	Min	–	–	–	–	–	–	–	–	–	–	–	–	Tensile Strength	655 MPa	–	114.3 mm (4.5″) to 406.4 mm (16″) / $d \geq 19$ mm	26.7 mm (1.05″) to 114.3 mm (4.5″) / $d \geq 19$ mm
	Max	0.43 Hardness	1.90	– 241 HBW 23 HRC	–	0.25	0.35	–	0.030	0.030	0.45	–	–	Yield Strength	552 MPa	655 MPa		
9Cr L80*	Min	–	0.30	0.90	8	–	–	–	–	–	–	–	–	Tensile Strength	655 MPa	–	114.3 mm (4.5″) to 339.7 mm (13.4″) / $d \geq 19$ mm	60.3 mm (2.38″) to 114.3 mm (4.5″) / $d \geq 19$ mm
	Max	0.15 Hardness	0.60	1.10 241 HBW 23 HRC	10	0.50	0.25	–	0.020	0.010	1.00	–	–	Yield Strength	552 MPa	655 MPa		
13Cr L80*	Min	0.15	0.25	–	12	–	–	–	–	–	–	–	–	Tensile Strength	655 MPa	–	114.3 mm (4.5″) to 339.7 mm (13.38″) / $d \geq 19$ mm	60.3 mm (2.38″) to 114.3 mm (4.5″) / $d \geq 19$ mm
	Max	0.22 Hardness	1.00	– 241 HBW 23 HRC	14	0.50	0.25	–	0.020	0.010	1.00	–	–	Yield Strength	552 MPa	655 MPa		
D6 1.4462**	Min	0.015	0.25	2.50	21	4.50	–	–	–	–	–	0.10	–	Tensile Strength	540 MPa	880 MPa	4.76 mm (3/16″) to 406.4 mm (16″) / $d \geq 19$ mm	–
	Max (X2CrNiMoN22 –35–3)	0.03 Hardness	2.00	3.50 26 HRC	23	6.50	0.25	–	0.035	0.015	1.00	0.22	–	Yield Strength	450 MPa	–		

*…all data according to API specification 5CT.
**… data acording ASME SA/ASTM A 789.

productivity at lower cost. The study shows that welding current plays a central role in optimising mechanical properties is suggested for the use of MIAB welding for high pressure applications in the energy and defence sectors (Suresh Isravel et al. 2020). Research by Kachinsky et al. on MIAB welding of seamless ASTM A106/API 5 L grade carbon steel pipe, which can be used in power plants, boilers, petrochemical plants, petroleum processing plants and ships, shows that future applications of pipe for liquids and gases under high pressure and temperature are possible. The test results show that the MIAB welded joints have high strength and good weld integrity at the level of the pipe base material. Thus, MIAB welding can be considered as a future fast and cost-effective welding process without expensive use of filler materials and shielding gas (Kachinskyi and Manurung 2021).

Materials and methods

Tube materials and geometries

Pipe geometries with an outer diameter of 47.8 mm and a wall thickness of 3.0 mm were used for forming the dissimilar joints via MIAB to simulate the materials combination of the borehole casing. Table 2 lists the materials used and their measured chemical compositions. The pipe sections each had a length of 150 mm. L80 Type 1 is a low-alloy steel which can be used in acidic environments. With its relatively high yield strength, this material can be used both as casing and tubing in deep wells. This material derives its strength from the ferrite/pearlite matrix and a fine-grained microstructure established during the manufacturing process. Thus, the material can lose its good properties due to increased grain coarsening at high temperature and low cooling rates. The material belongs to the quenched and tempered steels, and with a carbon equivalent of CEV = 0.64 it tends to harden in the heat-affected zone (HAZ) at excessively high cooling rates. The later typically result in the formation of martensite, but annealed bainite can also be present.

uplex steel 1.4462 is an austenitic-ferritic corrosion-resistant steel developed for oil and gas production in the North Sea. It offers excellent corrosion protection against media containing H_2S, CO_2 and Cl^- and is therefore ideally suited for the corrosion-prone areas of wells. It has almost equal microstructural proportions of ferrite (δ) and austenite (γ). The alloy is therefore characterized by increased strength as compared with pure austenite. Yet, the material features increased ductility and cyclic strength compared with purely ferritic or martensitic steels. Moreover, the material is very well suited for welding and can be processed by all major fusion welding methods.

MIAB-welding procedure

MIAB welds were performed on pipes in order to investigate the resulting mechanical properties and to carry out corrosion resistance studies of mixed L80 and duplex steel joints.

The pipe sections were welded on the system shown in Fig. 2 in a multi-stage process. First, the specimens were brought into contact using the linear motion axis. Next, the welding current was switched on and the specimens were moved apart a defined distance. This initiated the welding arc (drawn arc). The magnetic field unit then generated a magnetic field with the Lorenz force vector pointing in the circumferential direction. Thus, the resulting force acting on the arc column deflected it, such that the arc began to rotate around the tube end faces. In this manner, the surfaces at the pipe end sections were heated to above the melting temperature. Once this was achieved, the tube sections were pressed together with a defined and constant force of 130 MPa until the end of the solidification. With this process, the melt is forced out of the contact area to the inside and outside of the joining zone, and the weld bead is formed. Specifically, the contact zone experiences high pressure so that no solidified melt remains in the force-transmitting area, but the heat-affected zones of the pipe segments remain next to each other. Table 3 gives an overview of the selected welding parameters. To keep the heat input low, helium and oxygen containing gas mixtures were not used. Instead, the mixed gas M12-ArC-2 (98 vol.-% argon and 2 vol.-% carbon dioxide) was used for shielding.

Table 2
Chemical composition of the materials, measured by spark spectrometry.

Chemical composition in mass percent								
Material L80 Type 1								
C	Si	Mn	P	S	Cr	Ni	Cu	Al
0.36	0.22	0.91	0.006	0.002	1.01	0.1	0.11	0.032
Material 1.4462								
C	Si	Mn	P	S	N	Cr	Mo	Ni
0.03	1	2	0.035	0.015	0.15	22	3	5.5

Mechanical testing of the welded tube

The load bearing capacities of the hybrid welds were tested using a pipe expansion test according to the standard DIN EN ISO 8493 (DIN EN ISO 2004). In this test, the pipe is expanded at the welded end by pressing it into a mandrel. The test is carried out until a crack appears in the weld seam. The conical mandrel was made of hardened steel and had a polished and lubricated surface. The mandrel with a mandrel angle of 30° was fixed in a 230 kN universal testing machine and the crosshead speed was set to 10 mm/s. In accordance with the standard, the inner bead on the weld seam was removed by machining prior to testing. The outer bead was also turned flat until the weld surface was notch-free. In order to concentrate the load directly in the area of the weld, the pipe section of the side to be tested was cut off 2 mm above the weld, cf. Fig. 3. The expansion values of the individual materials were determined on unwelded pipe sections.

The percentage change of the diameter was determined from the ratio of D_u/D. A 30% drop in force on the testing machine was defined as the crack formation event.

Metallography

Cross-sections were prepared from the MIAB-welded hybrid joints using water-jet cutting, and then prepared for metallographic analysis. Using SiC abrasive paper, the preparation was carried out using grit sizes of 300, 600, 800, 1200 and 2000, followed by polishing with a diamond suspension to a surface roughness of 1 μm. To reveal the ferritic side of the L80 Type 1 material, the polished samples were etched with a 2% nitric acid. The duplex steel 1.4462 side was etched with Beraha II to reveal the microstructural constituents.

Corrosion testing

To evaluate the general corrosion properties, samples were cut from each section of the pipe (L80 base metal, L80 HAZ, welded area, duplex HAZ and duplex base metal, and samples with all zones). The samples were placed in a 5% NaCl solution and purged with CO_2. The duration of the immersion tests was 500 h.

Also, electrochemical studies of the samples were carried out in the CO_2 purged medium. For these studies, the samples with 12 mm x 5 mm x 4 mm were prepared using the same steps as described for the general corrosion tests. The samples were then insulated with a heat-resistant paint and varnish coating such that the area exposed to the electrolyte was ≈ 0.5 cm^2.

The electrochemical tests were performed using a VersaStat Princeton Applied Research potentiostat equipped with specialized software that allows to set different test cycles, sweep rates, and perform tests in potentiodynamic mode. For the investigations, a closed type of sealed cell was used with the possibility of gas saturation and thermosetting, cf. Fig. 4.

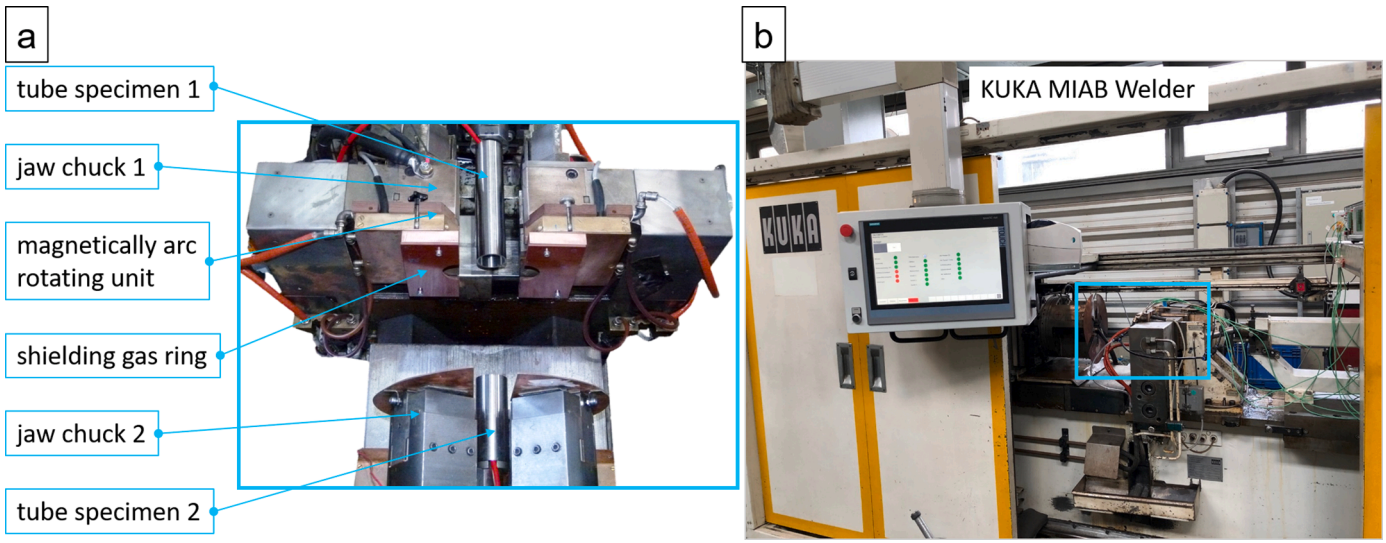

Fig. 2. Automatic MIAB welding system KUKA MagnetArc 5000/1000; a: detailed view of the clamping and welding device, b: overview of the MIAB welding machine.

Table 3
Welding parameters used to join the hybrid tube connection with MIAB.

KUKA MIAB Welding unit (KUKA H5000/1000)			welding parameter of the L80 Type 1 / 1.4462 hybrid MIAB weldment		
Prameter	Unit	Adjustment range	Ignition phase	Heating phase	Final phase
Welding current	A	50 - 1500	340	285	660 - 800
Arc voltage	V	20 - 40	28	25 - 27	30 - 40
Deflection coil current	A	1 - 25	12	8	12
Upset range	mm	1.5 - 3	2.3		
Upset time	s	≤ 0.5	≤ 0.5		
Protective gas flow rate	l/min	1 - 20	17.5		
Welding time	s	2 - 20	0.6	4.8	0.4
Area-related upsetting force	MPa	15 - 150	–	–	130

In the electrochemical tests, 300 ml of 5% aqueous solution of sodium chloride NaCl was employed as the electrolyte. All tests were carried out at ambient temperature (23 °C), and the cell was saturated by purging the solution with CO_2 prior to testing.

After immersing the test sample in the test cell, the open-circuit corrosion potential (E_{corr}) was measured for 55 min. Next, anodic polarization was carried out in potentiodynamic mode in the potential range from -300 to 1500 mV relative to E_{corr} with a sweep rate of 0.16 mV/s and a polarization curve was obtained. An Ag/AgCl electrode was used as the reference electrode, but all potential values provided in the following are with respect to the normal hydrogen electrode. The obtained polarization curves were used to determine the change in corrosion potential, the pitting formation potential, E_{pit}, and to calculate the theoretical corrosion rates by the Tafel method. The determination of the corrosion characteristics and all subsequent calculations were carried out in accordance with the standards ASTM G 3, G 5, G59, G61, ISO 17,475: 2005 and GOST 9.912–89.

Results and discussion

Hybrid L80 Type 1 / Duplex steel weldment

The welding parameters used for hybrid welding (see Table 3) led to successful welding of the different materials. As seen in Fig. 5(a), a

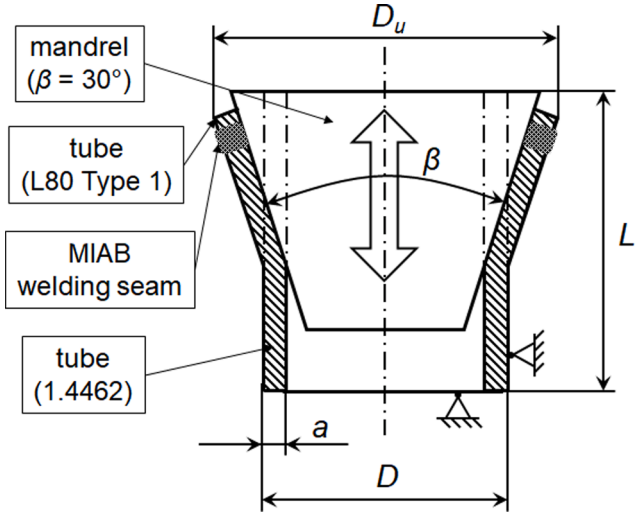

symbol	description	unit
a	tube wall thickness	mm
D	origin outer tube diameter	mm
D_u	maximum outer diameter after testing	mm
L	length of the tube before testing	mm
β	angle of the conically mandrel	degree

Fig. 3. Description of the tube expansion test procedure according DIN EN ISO 8493 (DIN EN ISO 2004).

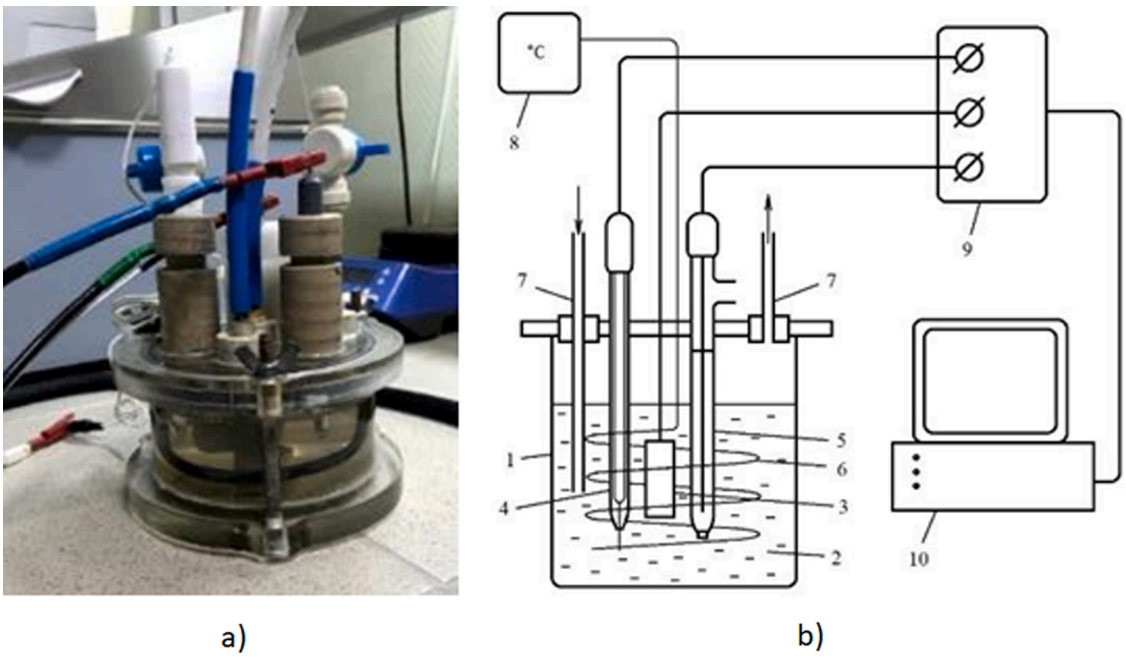

Fig. 4. Electrochemical cell: a) general view, b) diagram of an electrolytic cell: 1 - clamping cell, 2 - electrolyte, 3 - working electrode, 4 – platinum counter electrode, 5 - reference electrode, 6 - heater winding, 7 - gas saturation system, 8 - thermostat, 9 - potentiostat, 10 - computer with software.

welding bulge typical for MIAB welding was formed both on the outside and inside of the pipe joint. The bead extends approx. 2.5 to 3 mm circumferentially inwards and outwards and the pipes are well aligned. The difference in the tarnishing colours on the outer surfaces of the specimens reflects the different properties of the two materials, cf. Fig. 5 (a). The different thermal conductivities ($k_{\text{L80 Type 1}}(20\ \text{K}) = 43$ W/mK (siJ group 2016); $k_{1.4462}(20\ \text{K}) = 14$ W/mK (Deutsche Edelstahlwerke 2007)) of the two materials results in differences in heat dissipation of the welding heat generated in the arc process. The heat is dissipated much faster in the L80 Type 1 steel than in the duplex steel. Due to the duration of the welding process of 5.6 s and the subsequent cooling, the duplex steel is only heated to a very small extent, as heat conduction is curtailed there. By using a mixture of argon with CO_2 during MIAB, this is mapped very clearly, as oxygen is available for oxide formation.

The mechanical test and the test results are shown in Fig. 5(b) and Fig. 6. When the duplex steel was in contact with the test cone, the tube expanded without failure up to the possible maximum force of 230 kN and plastic deformations in the 29 to 31% range were obtained (see Fig. 6a). Since the maximum load capability of the testing machine was reached before component failure, the break-off criterion was not yet reached, and thus no maximum elongation can be given here. The force-displacement curve reproducibly shows a clear range of elastic deformation. After exceeding the yield point of the material (1.4462), plastic deformation increases almost linearly up to the maximum force value. Both at 5% and 10% total elongation, fluctuations in the force-displacement curve are seen, which can be explained by settling movements between the tube and the test cone and are caused by a stick-slip effect between the friction partners.

When the L80 Type 1 steel is in contact with the test cone, a different material behaviour emerges. After the region of elastic deformation, the tube expanded plastically and at a certain force the failure criterion was always reached, so that the test was terminated. Maximum forces of approx. 122 to 138 kN were reached. The maximum plastic deformation due to the expansion was 17.5 to 20% and the plastic behaviour is essentially linear on the force-displacement curve. Minimal settling movements due to the stick-slip effect can also be seen here (Fig. 6, b).

Upon comparing the behaviour with the non-welded condition, only a minimal reduction in ductility upon welding became obvious for the

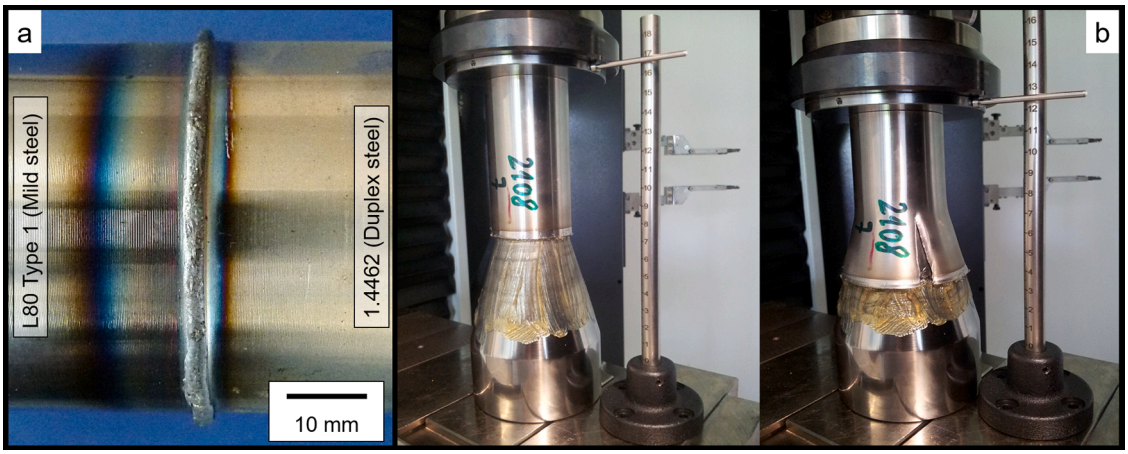

Fig. 5. Colouring of the welds indicating the difference in heat dissipation of the two materials (a); test set-up used for expansion testing of the pipe joints (b).

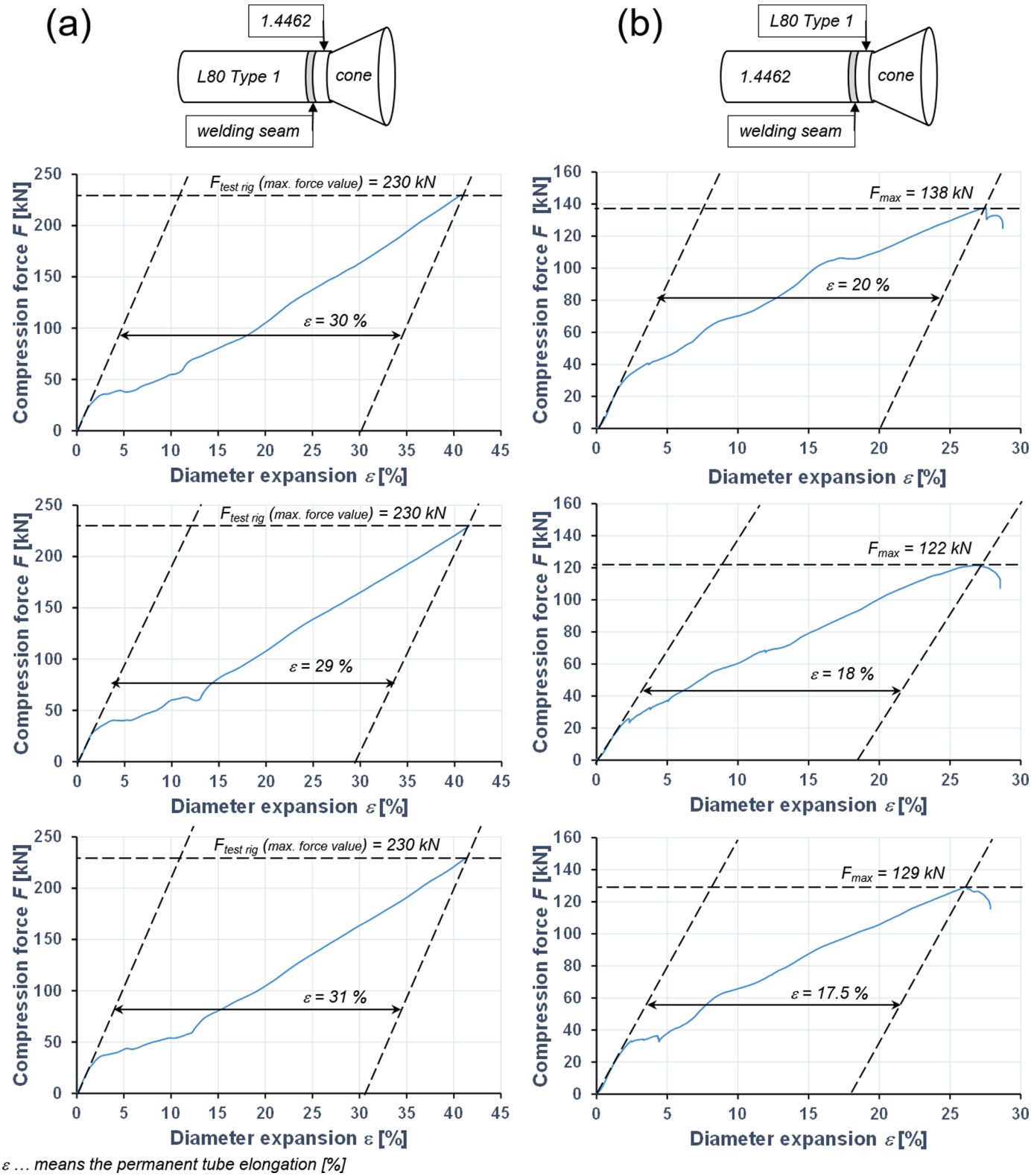

Fig. 6. Mechanical properties of the hybrid pipe joints as a function of the test direction (a: expansion of 1.4462; b: expansion of L80 Type 1).

L80 Type 1 steel. Whereas the non-welded condition featured a plastically diameter expansion of (23 ± 2.0%), the welds always failed in the 22 ± 2.5% range (Fig. 6, b and Fig. 7, b, d). In contrast, the duplex steel showed only a minor effect, as the plastic expansion of (37 ± 3%) for the non-welded material was not fully reached in the welded condition (33 ± 1.2%) (Fig. 6, a and Fig. 7, a, c).

Fig. 7 shows the total elongation in the test as well as the representation of the plastic and elastic components. It is clear that the 1.4462 side tolerates a much greater plastic deformation than the L 80 Type 1 side. However, the elastic recovery is greater for the 1.4462 than for the L 80 Type 1. The distribution of the measured values is much greater for the 1.4462 side than for the test from the L 80 Type 1 side.

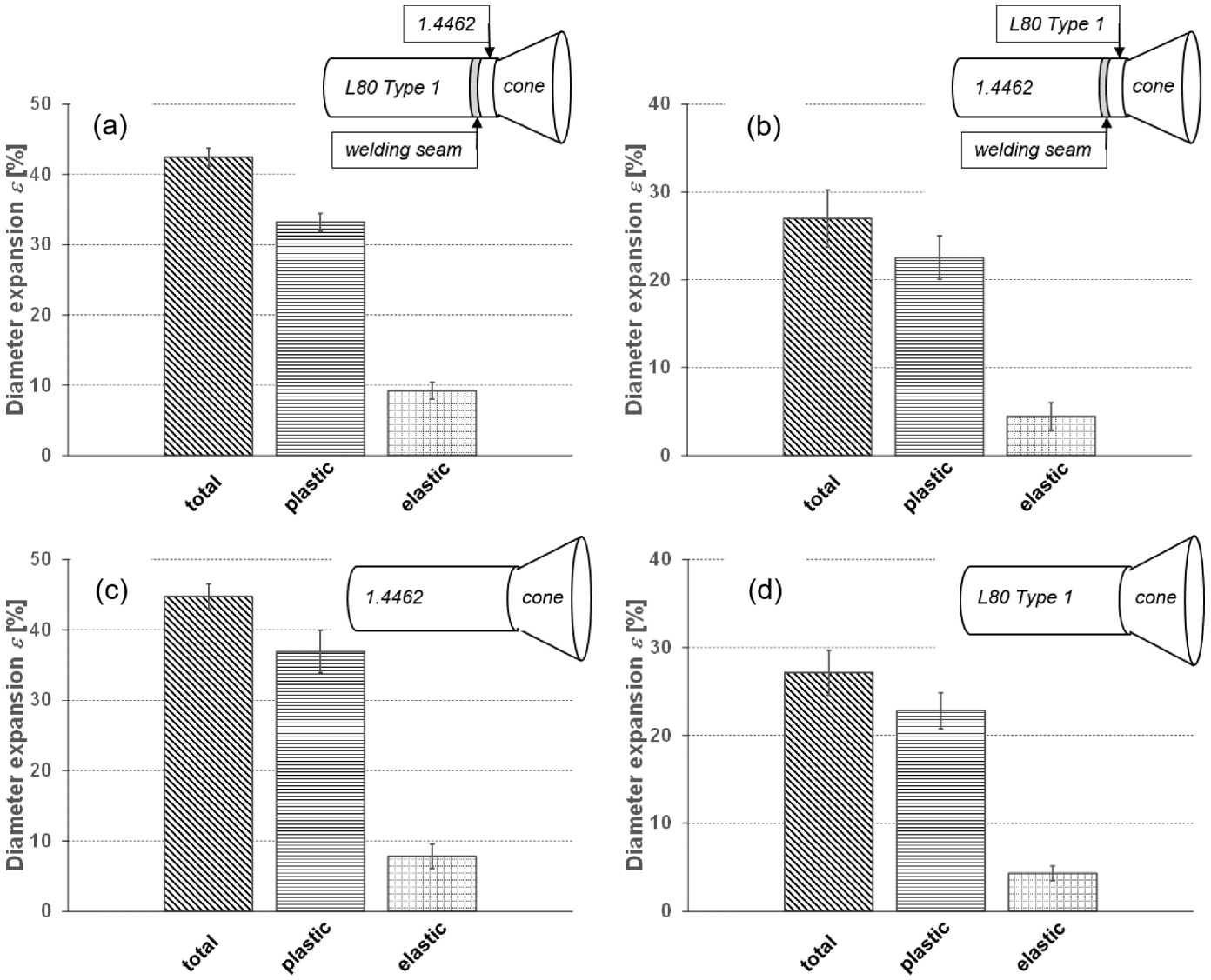

Fig. 7. Overall representation of the percentage strains for the pipe expansion tests (a: 1.4462 side, $N = 8$; b: L80 type 1 side, $N = 18$; c: 1.4462 base material, $N = 6$; d: L 80 Type 1 base material, $N = 8$).

The reduction in the deformability of the L80 Type 1 steel can be attributed to the accelerated cooling after welding. Due to the high CEV, an essentially martensitic/bainitic microstructure was formed in the heat-affected zone, whereby the good deformation properties of the initial ferritic/perlitic microstructure are lost. Due to the low heat input into the duplex steel, no significant transformation took place there and the ferrite remained largely unaffected. Only the plastic deformation of the material associated with the pressing process has a ductility-reducing effect here (see Fig. 8a-g).

The cross-section of the hybrid joint shows a clear joint line at which a material bond is formed between the two materials. The flow movement that the material underwent during the upsetting process is clearly visible (Fig. 8a). Both the pearlite lines of the L80 Type 1 and the ferrite lines of the duplex steel are deflected towards the outside as well as the inside of the pipe. This shows that the arcing process has produced melt on both sides, which was then pressed out of the joining area such that the two materials are finally joined in the heat-affected zones. The external beads thus represent the displaced molten material, which does not contribute to the force transmission of an MIAB welded joint. The pores and slag inclusions that may be enclosed there can be easily removed by machining, at least in the outer area. Clearly, there are no solidified areas in MIAB weld, which would result in unfavourable mixtures of the two materials. Yet, it is noticeable that there are discrete areas of austenitic material on the side of the L80 Type 1 steel within the joint zone (Fig. 8c, d, f, g). This can be explained by the melting dynamics during the arc firing phase. Since welding takes place in a horizontal position, the molten material follows the acting gravitational force, sags downwards, and flows together. The arc, which is rotated by the magnetic field in a fixed direction around the pipe end faces, cyclically pushes this area of melt out of the direction of flow and creates waves on the surface of the molten pool. This turbulence in the melt leads to mutual contact of the wave crests on both sides and initiates melt pool contact and also short circuits. In the process, molten areas of both materials merge. Due to the very short welding time of only a few seconds in total, of which the molten state is only reached in the last third, only a minimal metallurgical mixing of the two materials takes place, which can be found in the outer areas of the bead after pressing. Inside, the areas enclosed and not mixed by the pressing remain, but do not pose any problem with regard to the mechanical properties.

The MIAB welding process affects the materials through the heating and cooling cycle, which is the main reason for the change in material properties. The ferritic/perlitic L80 Type 1 steel with a CEV of 0.64, which is essentially in eutectoid composition, receives its excellent strength and ductility properties during the heat treatment during pipe

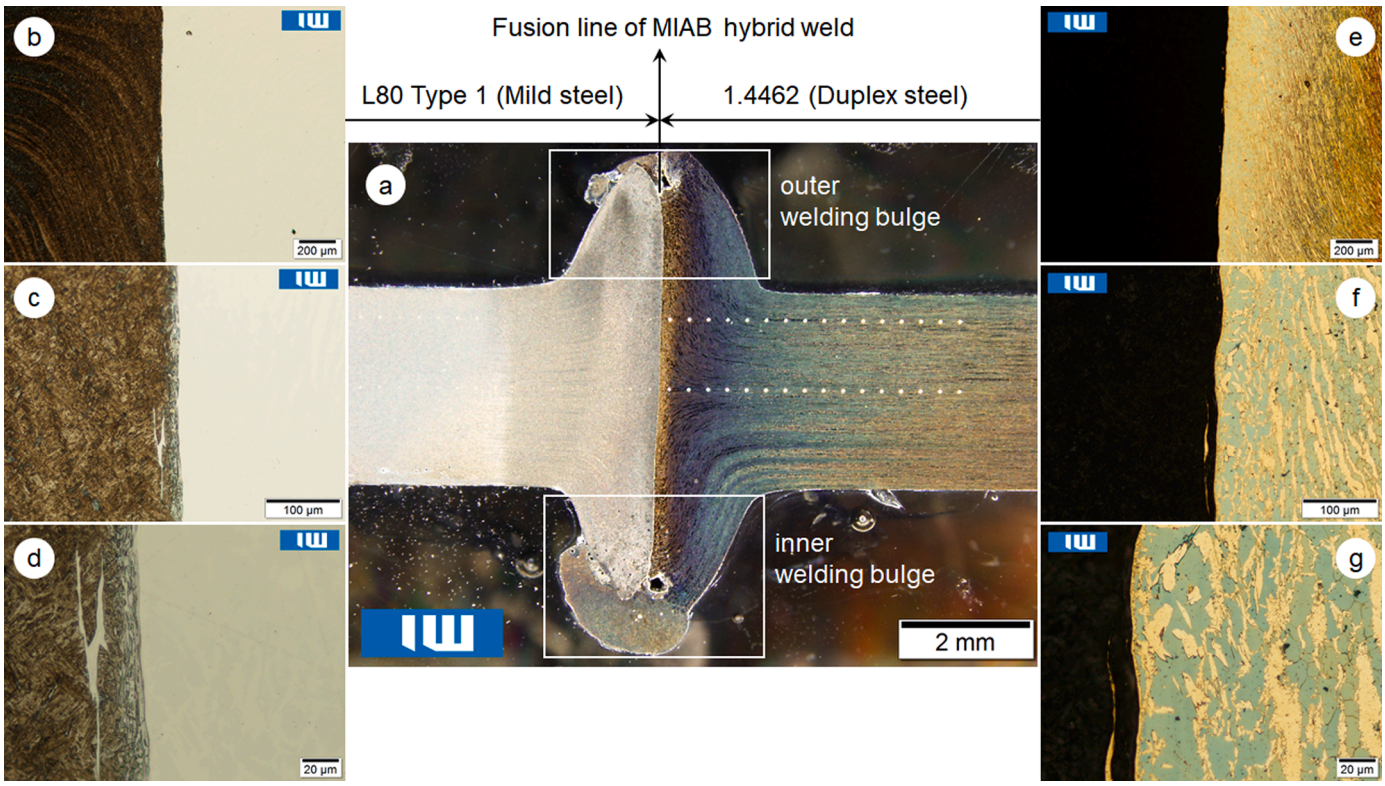

Fig. 8. Cross-section of a hybrid joint: overview in (a) and higher magnification details prepared to highlight the microstructure of the L80 Type 1 in (b-d) and the duplex steel in (e-g).

manufacture. In the normalised condition, L80 Type 1 is equivalent to a hypo-eutectoid steel, which consists of ferrite and pearlite. As this is only valid for slow cooling, the microstructure of the heat affected zone and the weld zone of L80 Type 1 do no longer show this type microstructure. Instead, the rapid cooling produces a martensitic/bainitic structure, which shows much higher strengths with simultaneously decreasing ductility. This is obvious in Fig. 8(a), where the transformation zone protrudes ≈ 2.5 mm into the base material. The microstructure there (Fig. 8b, c, d) features a needle-like structure, which does not show any discrete grain boundaries or ferrite/pearlite regions. The acicular structure is not as pronounced as in a pure martensitic steel and can be interpreted as tempered martensite. Due to the heat cycle in the welding process, a clear change in the microstructure is also recognisable in the area of the joining zone on the L80 Type 1 side. Here, it can be assumed that the rapid cooling leads to a transformation of the initial ferritic/perlitic microstructure into the bainite. This is clearly visible in the hardness profile, whereby the highest hardness was measured directly at the joining zone with (450 ± 30) HV1. Over the darker area of the heat-affected zone of the L80 Type 1 (Fig. 8(a)), the hardness then drops continuously to the value of the base material of (237 ± 5) HV1. This explains the decrease in ductility in the expansion test by ≈ 20% for the L80 Type 1 steel. As the microstructural changes can be reversed, it can be assumed that an improved in ductility would be obtained by an additional heat treatment of the weld.

The duplex steel shows a completely different behaviour with regard to the microstructural changes. Directly at the joining zone, in the area where high temperatures prevail, an approximately 250 µm wide zone rich in δ-ferrite is formed. δ-ferrite solidifies primarily and is almost completely retained due to the (relatively) fast heat dissipation by the close contact with the L80 Type 1 material. This is clearly visible in Fig. 8 (a, e, f, g), where the etching method makes the δ-ferrite appear yellowish (bright) and the formed austenite bluish (dark). This results in a very narrow but completely continuous δ-ferrite fringe directly at the contact point (see Fig. 8f, g). This 2–3 µm wide fringe forms a complete interface between the two materials. Given the small size, it does not lead to the high brittleness typical for higher δ-ferrite contents. It must be noted, however, that type of the ferrite line formation, which is known for MIAB welding, is strongly parameter-dependant, which in turn calls for accurate process control.

At a distance of approx. 100 µm from the joining zone, an evenly distributed and non-directional ferrite/austenite microstructure can be observed, which is a microstructure generated by the welding heat and formed only after the upsetting process (see Fig. 8e, f, g). This is followed by the deformed initial microstructure, which has not been transformed by the welding process. This part can be identified by the clear deflection of the grain structure of the δ-ferrite/austenite grains by ≈ 75° As expected from Fig. 8 (a-d), the heat-affected zone on the duplex side is much smaller than on the L80 Type 1 side as most of the welding heat is dissipated via the L80 Type1 due to its higher thermal conductivity.

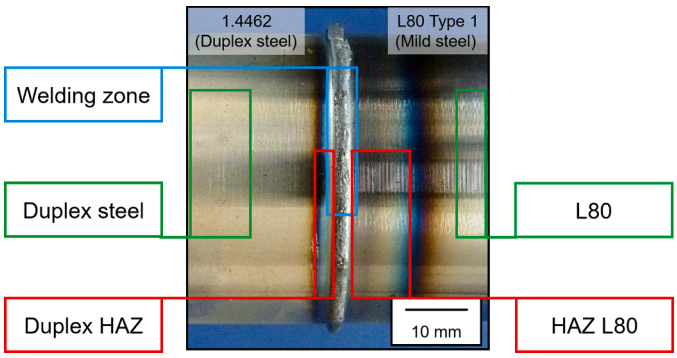

Fig. 9. Macroscopic appearance of full size samples after corrosion testing.

Corrosion results

Fig. 9 shows a full size sample after corrosion testing with the different test sections being highlighted. However, as seen in Fig. 8(a), the sizes of the heat-affected zones are small. Thus, test sections from the heat-affected zones encompassed additional material. Still, when the samples are corroded, the part of the material that has the least resistance to corrosion, reacts most actively with the electrolyte. Thus, it is still possible to obtain comparative data on corrosion rates and useful values of electrochemical parameters. In Fig. 9 it can be seen that there are no apparent corrosion products on the duplex steel, on its heat-affected area and on the duplex steel part of the weld zone sample, i. e. only the L80 steel part is significantly affected by corrosion.

Based on the appearance of the samples after testing, general corrosion dominated. However, the presence of some pits can be noted over the entire area of the L80 part of the sample. Part of these can be attributed to the initial grinding of the samples. The slight increase in the number of pits at the weld zone is associated with the contact of materials with different potentials.

The data from the general corrosion tests and from the electrochemically controlled tests are summarized in Table 4 and Table 5, respectively. Both types of test reflect the difference in the individual material properties and demonstrate that the weld seam is more prone to corrosion attack than the rest of the samples. Geometrically, the susceptibility to corrosion begins with the metallurgical transition from duplex steel to L80, which results in an increase in the corrosion rate by 2 orders of magnitude. The weld seam itself appears to be more susceptible to corrosion. This can be explained by the fact that the contact to the duplex steel is present in the weld area and therefore the local element is directly effective. Thus, not only the heat treatment condition and the microstructure influence are reflected there, but also the electrochemical contact element. If this is not present, however, the corrosion rate decreases only slightly, so that the L 80 side is at greater risk of corrosion than the duplex side.

Fig. 10 shows the evolution of the open-circuit potential with time for the different material sections. The curves indicate that the environmental conditions did not vary significantly over time. The more negative potential values of the L80 material are in line with its higher overall corrosion rate.

From Fig. 10, it is not only clear that there is a substantial difference in electrochemical behaviour between the L80 steel and the duplex one, but that the L80 clear dominates the response of the weld seam.

Moreover, it can also be noted that, in comparison with the unaffected duplex steel, the corrosion resistance of the HAZ of the duplex steel is slightly worse. This can be attributed to the thermal effects resulting in δ-ferrite appearing during welding in the HAZ, which in turn reduces the corrosion properties of the duplex steel.

In Fig. 11 shows polarization curves in logarithmic coordinates at different scales, obtained during the anodic linear polarization of the samples under study.

Based on the polarization curves constructed in logarithmic coordinates using the Tafel curve (oblique) method and Faraday's law

Table 4
Mass loss in the corrosion tests.

Marking	Average corrosion rate; g/m2h	Average corrosion rate; mm/a	Comments
Duplex base metal	0.0007	0.0008	No corrosion.
Duplex HAZ	0.0038	0.0042	Increased corrosion rate.
Weld metal	0.0719 (0.1208)	0.0802 (0.1348)	Significant increase of the corrosion rate, but in terms of area below of the rate of low alloy steel.
HAZ / L80	0.0906	0.1011	Lower corrosion rate than into the weld metal.
L80 / Base metal	0.0827	0.0923	Lower corrosion rate than into the weld metal and HAZ.
Full sample	0.0668 −0,125	0.0746 (0.1394)	Similar to the weld metal. The values in brackets is given taking into account corrosion of only the L80 part of the hybrid sample.

Table 5
Characteristic potentials and corrosion rates obtained in the electrochemically controlled tests.

Marking	Open circuit potential; mV	Corrosion rate; mm/a	Pitting corrosion potential; mV
Duplex base metal	145	0.0021	1207
Duplex HAZ	-151	0.0054	1051
Weld metal	-633	0.527	—
HAZ / L80	-612	0.264	—
L80 / Base metal	-593	0.284	—

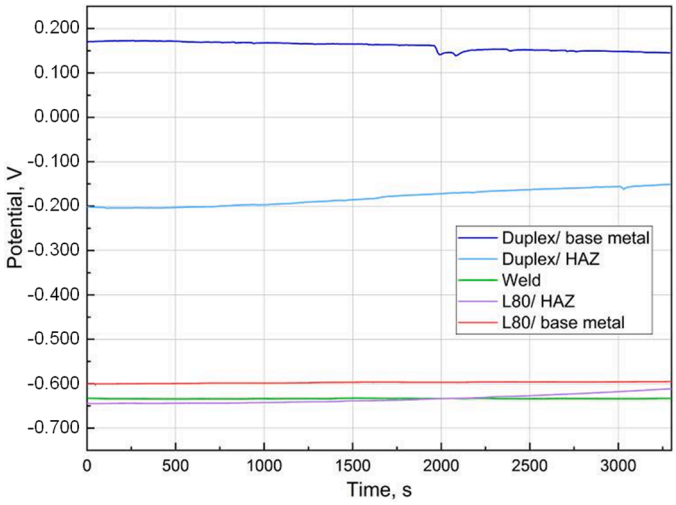

Fig. 10. Evolution of the corrosion potential (Open circuit potential) upon testing in 5% NaCl solution purged with CO_2.

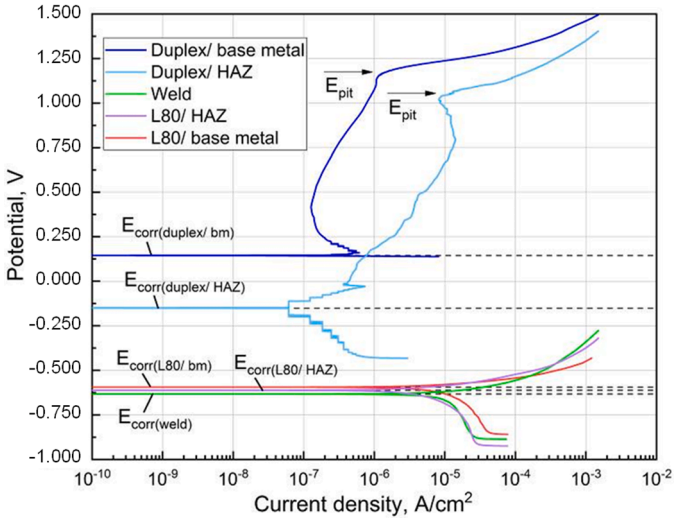

Fig. 11. Polarization curves of the samples with a semi-logarithmic scale.

(ASTM G102), the theoretical corrosion rates were calculated, the values of which are presented in Table 5. In this work, the theoretical corrosion rates were calculated using the VersaStudio software to the VersaStat potentiostat.

Fig. 10 shows that the corrosion potential of the L80 base metal is only marginally higher than for the weld. The difference is only 40 mV, which again demonstrates that the corrosion properties of the hybrid connection are dominated by the ignoble character of the LH80 material. Thus, no plateau of passivity is observed in either case on the anodic branch of the polarization curves. Instead, a sharp increase in the current in both the anode and cathodic branch is see, resulting in high values for the corrosion upon calculating the intersection of the Tafel curves.

In Fig. 10, a nearly constant current can be observed in the potential range from ≈ 150 mV to ≈ 1100 mV for the sample from the duplex base metal (dark blue line). This shows that the sample has formed a passive oxide layer and, as a result, has high corrosion resistance. Based in the pitting potential E_{pit} (breakdown), at which a sharp increase in current occurs, it is possible to compare the corrosion resistance of the HAZ and the base metal of the duplex steel. The higher the pitting potential, the better corrosion resistance (stability of the oxide) the material has. Accordingly, the base metal of the duplex steel has a higher corrosion resistance (E_{pit} = 1207 mV) compared to the HAZ of duplex steel with E_{pit} = 1051 mV. Still, the HAZ of the duplex steel features excellent corrosion resistance, and in contact with the LH80-dominated weld, material galvanic corrosion will degrade the LH80 side.

Conclusion

In the present study magnetically impelled arc butt welding (MIAB) was used to form hybrid joints between tubes made from L80 Type 1 steel and a 1.4462 duplex steel. The main results can be summarized as follows:

1 Using the MIAB process, L80 Type 1 and 1.4462 duplex steel can be successfully welded, with acceptable mechanical properties for casing and deep drilling applications. The direct welding of the two different materials thus enables a change of material in the casing, for example to stabilise layers with a sulphuric acid environment in the borehole. Contact with hydrogen sulphide leads to a strong corrosive attack on L 80, whereas duplex steel is resistant.
2 Without additional heat treatment, the ductility of the LH 80 part as determined in pipe expansion test is comparable to the base material. This offers the possibility to uses such welding connections without additional heat treatment processes.
3 On the duplex side, there is no significant change in microstructure and resulting properties due to the joining process.
4 The heat-affected zone of the duplex steel demonstrates slightly inferior corrosion resistance as compared to the virgin material. However, the electrochemical properties of the weld are clearly dominated by the LH80 Type 1 material, and the corrosion tests revealed negligible corrosion attack of the duplex part of the hybrid joint.
5 The welding technology presented here for the realisation of a hybrid connection using the MIAB technology of Duplex steel and L 80 steel opens up the prospect of dispensing with the cost-intensive and time-consuming pipe fitting by means of sleeves. In addition, this technology can lead to considerable time savings during the installation of the casings, as the preparatory work steps of thread production and the manufacture of the sleeves themselves can be eliminated by pipe-to-pipe welding. In addition, this technology enables greater robustness against leaks in the casing.

Acknowledgement

The research was supported on the German side within the framework of the Lower Saxony Research Network "Geothermal Energy and High-Performance Drilling Technology" (GeBo) funded by the Lower Saxony Ministry of Science and Culture (project no. ZN2481GeBoW5 and ZN2481GeBoW6) and from the Russian side by the Ministry of Science and Higher Education of the Russian Federation as part of World-class Research center program: Advanced Digital Technologies (contract No. 075–15–2020–934 dated on 17.11.2020)

References

Alekseeva, E., Karasev, A., Jönsson, P.G., Alkhimenko, A, 2020. Effect of inclusions on the corrosion properties of the nickel-based alloys 718 and EP718. Metals (Basel) 10 (9), 1177.
Alkhimenko, A., 2019. Corrosion testing of experimental steels for oilfield pipelines. E3S Web Conf. 121, 1001.
API American Petroleum Institute, 2021. 5CT Specification for casing and tubing. Am. Petroleum Institute.
Bérest, P., Réveillère, A., Evans, D., Stöwer, M., 2019. Review and analysis of historical leakages from storage salt caverns wells. Oil Gas Sci. Technol. – Rev. IFP Energies nouvelles 74, 27.
Balta, Berna, Arıcı, Aziz Armağan, Yılmaz, Muharrem, Gümüş, Serap, Yücel, Selçuk Can, 2018. Microstructural and mechanical properties of friction and MIAB welded carbon steel tubes and forging bracket joints. Mater. Testing 3, 273–282 https://www.degruyter.com/document/doi/10.3139/120.111144/html.
Davydov, A., Alekseeva, E., Gaev, A., 2020. Specificity to the choice of materials for wellhead equipment. Mater. Today: Proceedings 30, 549–553.
Deutsche Edelstahlwerke. 2007. Datenblatt_4462_UK_. Stainless duplex austenitic-ferritic, chromium nickel molybdenum steel. https://www.dew-stahl.com/fileadmin/files/dew-stahl.com/documents/Publikationen/Werkstoffdatenblaetter/RSH/Datenblatt_4462_UK_.pdf.
Dhivyasri, G., Rahul, S.G., Kavitha, P., Arungalai Vendan, S., Ramesh Kumar, K.A., Gao, L., and Garg, A. 2018. Dynamic control of welding current and welding time to investigate ultimate tensile strength of miab welded T11 tubes. J. Manuf. Process32, 564–581. https://www.sciencedirect.com/science/article/pii/s1526612518301531.
DIN EN ISO, 2004. Metallic materials - Tube - Drift-expanding test (ISO 8493:1998). German Version EN ISO 8493:2004. Beuth Verlag, Berlin. DIN EN ISO 8493.
Faes, K., Dhooge, A., Baets, P.de, Afschrift, P, 2009. New friction welding process for pipeline girth welds—Welding time optimisation. Int. J. Adv. Manuf. Technol. 43 (9–10), 982–992.
Faes, K., Dhooge, A., Jaspart, O., D'Alvise, L., Afschrift, P., Baets, P.de., 2007. New friction welding process for pipeline girth welds - parameter optimization. Proceedings of the Institution of Mech. Eng. Part B: J. Eng. Manuf. 221 (5), 897–907.
Fruhwirth, R.K., Hofstätter, H., 2016. An innovative approach for optimising geothermal energy recovery /Tiefe geothermische Energiegewinnung - Innovative Wege zur Optimierung. Geomechanik Tunnelbau 9 (5), 489–496.
Galle, T., Waele, W.de, Baets, P.de, van Wittenberghe, J., 2011. Influence of design features on the structural integrity of threaded pipe connections. Sustainable Construction and Design 2011 (SCAD) 2 (2), 237–245 https://biblio.ugent.be/publication/1176947.
Ganesan, S.M., Moe, P.T., Vinothkumar, P., Audestad, J.I., Salberg, B., Valberg, H., Solberg, J.K., Burnell-Gray, J.S., Rudd, W, 2010. Establishment of heat treatment cycles for forge welded API L80 tubular joints. Int. J. Mater. Form 3, 343–346. S1.
Hassel, T., Varahram, A., Baer, F., Mitulla, S., Lehr, J., Overmeyer, L.L.J., Wohlgemuth, H.L., Bach, F., Brouwer, D., 2016a. Arc guiding, gripping and sealing device for a magnetically impelled butt welding rig. United States Patent. Google Patents. US 9308600 B2.
Hassel, T., Varahram, A., Benedict, D., Lehr, J., Bach, F.W., 2016b. Enhanced magnetically impelled arc butt wielding (MIAB) technology. United States Patent. Google Patents. US 9446470 B2.
JFE Steel Corporation, 2021. OCTG. Oil Country Tubular Goods https://www.jfe-steel.co.jp/en/products/pipes/catalog/e1e-012.pdf.
Kachinskiy, V.S., Krivenko, V.G., Ignatenko, V.Y., 2002. Magnetically impelled arc butt welding of hollow and solid parts. Weld World 46 (7–8), 49–56.
Kachinsky, V.S., Kuchuk-Yatsenko, S.I., 2017. Joint formation in magnetically-impelled arc butt welding of thick-walled pipes from high-strength steels. The Paton Welding J. 8, 39–45, 2017,.
Kachinskyi, V.S., Manurung, Y.H.P., 2021. Investigations of the quality of welded joints of pipes from steel of ASTM A106/API 5L grade, using magnetically impelled arc butt welding. Paton Welding J. 11, 9–14.
Kostitsyna, I., Shakhmatov, A., Davydov, A., 2019. Study of corrosion behavior of carbon and low-alloy steels in CO 2 -containing environments. E3S Web Conf 121, 4006.
Kovalev, M., Shakhmatov, A., Alhimenko, A, 2020. Electrochemical studies of welded joints corrosion resistance made from stainless steels. Mater. Today: Proceedings 30, 501–505.
Li, L.F., 2013a. Corrosion-resistant alloys for tubings and casings and alloy material selection in oil and gas wells. AMR (690–693), 276–279.
Li, L.F., 2013b. Research on tubing and casing corrosion in sour gas reservoirs and corrosion-resistant material selection. AMR (690–693), 1516–1519.
Li, L.F., Liu, X.M., Huang, Z.Q., 2012. Study and application for corrosion-resistant material selection of tubing and casing in sour gas reservoirs under coexistence of H2S and CO2. AMR 485, 429–432.

Moe, P.T., Salberg, B., Rabben, K., Halmrast, B., Audestad, J.I., Burnell-Gray, J.S., Rudd, W, 2010. Shielded active gas forge welding – from laboratory to field experiments. Int. J. Mater. Form 3, 1027–1030. S1.
Oppelt, J., Lehr, J., 2012. Innovative drilling and completion concept for geothermal applications. In Innovative Drilling and Completion Concept for Geothermal Appl. 109–114.
Palanisamy, V., Solberg, J.K., Moe, P.T., 2021. Shielded active gas forge welding of an L80 steel in a small scale shielded active gas forge welding machine. JMMP 5 (1), 16.
Panda, B.N., Vendan, S.A., Garg, A., 2017. Experimental- and numerical-based studies for magnetically impelled arc butt welding of T11 chromium alloy tubes. Int. J. Adv. Manuf. Technol. 88 (9–12), 3499–3506.
Ren, C., Zeng, D., Lin, J., Shi, T., Chen, W, 2012. Sour corrosion of C110 steel and its influence by galvanic couple and stress. Ind. Eng. Chem. Res. 51 (13), 4894–4904.
Sedmak, A., Arsić, M., Šarkoćević, Ž., Medjo, B., Rakin, M., Arsić, D., Lazić, V., 2020. Remaining strength of API J55 steel casing pipes damaged by corrosion. Int. J. Pressure Vessels and Piping 188, 104230.
siJ group. 2016. SIQUAL 7033 Steel (Mat.No. 1.7033, DIN 34Cr4, AISI 5132). (L80 Type 1 equivalent). https://steelselector.sij.si/data/pdf/VC130.pdf.
Sun, Y.X., Lin, Y.H., Wang, Z.S., Shi, T.H., 2012. Casing and tubing design for sour oil and gas fields. Pet. Sci. Technol. 30 (9), 875–882.
Suresh Isravel, R., Saravanan, S., Venkateswaran, P.R., 2020. Exploration of magnetically impelled arc butt welded SA210GrA tubes for boiler applications. Mater. Today: Proceedings 21, 123–126.
Teodoriu, C., 2015. Dynamic casing shoe while drilling: a smart drilling concept for future monobore technologies. J. Nat. Gas Sci. Eng. 27, 1279–1286.
T.P.S. technitube Röhrenwerke GmbH. 2017. Seamless tubes catalog.
Varahram, A., Breidenstein, B., Hassel, T., Bach, F.-.W., Maier, H.J., 2014. New design and construction of expandable casing tubes. Forsch Ingenieurwes 78 (3–4), 145–149.
Vendan, S.A., Kamal, R., Karan, A., Gao, L., Niu, X., Garg, A., 2020. Supervised Machine Learning in Magnetically Impelled ARC BUTT Welding (MIAB). In Welding and Cutting Case Stud. Supervised Machine Learn. 1–56.
Vendan, S.A., Manoharan, S., Nagamani, C., 2012. MIAB welding of alloy steel tubes in pressure parts: metallurgical characterization and non destructive testing. J. Manuf. Process 14 (1), 82–88.
Vinothkumar, P., Ganesan, S.M., Solberg, J.K., Salberg, B., Moe, P.T., 2011. Studies on shielded active gas forge welded API 5CT L80 material at different cooling rates. AMR 409, 871–876.